# A 3D time-dependent backward erosion piping model

Pol, Johannes C.; Noordam, Aron; Kanning, Willem

**DOI**
10.1016/j.compgeo.2024.106068

**Publication date**
2024

**Document Version**
Final published version

**Published in**
Computers and Geotechnics

**Citation (APA)**
Pol, J. C., Noordam, A., & Kanning, W. (2024). A 3D time-dependent backward erosion piping model. *Computers and Geotechnics*, *167*, Article 106068. https://doi.org/10.1016/j.compgeo.2024.106068

Computers and Geotechnics 167 (2024) 106068

Contents lists available at ScienceDirect

Computers and Geotechnics

journal homepage: www.elsevier.com/locate/compgeo

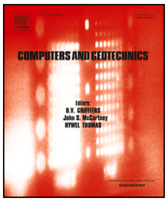

Research paper

# A 3D time-dependent backward erosion piping model

Johannes C. Pol [a,b,*], Aron Noordam [c], Willem Kanning [a,c]

[a] Department of Hydraulic Engineering, Delft University of Technology, Stevinweg 1, 2628 CN Delft, The Netherlands
[b] HKV, Botter 11-29, 8232 JN Lelystad, The Netherlands
[c] Unit Geo-engineering, Deltares, Boussinesqweg 1, 2629 HV Delft, The Netherlands

## ARTICLE INFO

*Keywords:*
Internal erosion
Backward erosion piping
Sediment transport
Finite elements

## ABSTRACT

Backward erosion piping (BEP) is a failure mechanism of hydraulic structures like dams and levees on cohesionless foundations subjected to seepage flows. This article models the time-dependent development of BEP using numerical simulation of the erosion process. A 3-dimensional finite element equilibrium BEP model is extended with a formulation for the sediment transport rate. The model is compared to and calibrated with small- and large-scale experiments. Finally, a large set of simulations is analyzed to study the effects of factors such as grain size, scale (seepage length) and overloading on the rate of pipe progression. The results show that the development of BEP in the small-scale experiments is predicted well. Challenges remain for the prediction at larger scales, as calibration and validation is hard due to limited large-scale experiments with sufficiently accurate measurements. The results show that the progression rate increases with grain size and degree of overloading and decreases with seepage length, which is consistent with experimental observations. The model results provide a better physical basis for incorporating time-dependent development in the risk assessment and design of levees.

## 1. Introduction

Backward erosion piping (BEP) is a geotechnical failure process by which groundwater flow under a structure erodes the granular foundation which is covered by a cohesive layer (Fig. 1). This may occur both at rigid structures such as weirs or sluices (Bligh, 1910) and at soil structures like embankments or dams (Foster et al., 2000). Research over the past decades has led to an increased understanding of the processes involved in BEP (Miesel, 1977; Hanses, 1985; Sellmeijer, 1988; Schmertmann, 2000; Van Beek, 2015; Vandenboer, 2019; Xiao et al., 2019a) This involves among others the interplay between groundwater flow in an aquifer, flow in micro-scale channels or pipes, primary erosion of the soil at the pipe tip (pipe lengthening) and secondary erosion (pipe deepening and widening), see Fig. 1. The research, and the resulting predictive models, focused primarily on the critical conditions for BEP to develop: the critical head $H_c$. More recently, there is an increasing amount of research into time-dependent aspects of the erosion process, both experimentally (Allan, 2018; Vandenboer et al., 2019; Robbins et al., 2017, 2020; Pol et al., 2022) and using numerical modeling (Wang et al., 2014; Rotunno et al., 2019; Wewer et al., 2021). This is especially relevant for BEP risk assessments of hydraulic structures when the hydraulic load is shorter than the time scale of the erosion process from initiation to catastrophic failure. Furthermore, insights in the time scale of the failure process, and how that depends on local factors, may inform emergency response decisions when initiation of failure is observed. Such applications need a predictive model to translate experimental results to field conditions. These models can be empirical (Pol et al., 2019), semi-analytical (Kézdi, 1979), based on finite elements (Wang et al., 2014; Rotunno et al., 2019; Wewer et al., 2021) or discrete elements (Tran et al., 2017). Steady-state 3-dimensional models can yield significantly different results compared to 2-dimensional models, for instance due to seepage from the sides (Vandenboer et al., 2014), meandering and branching (Robbins and Griffiths, 2018) and more severe flow concentration near the pipe tip (Van Beek et al., 2022). These 3D-aspects are expected to affect time-dependent extensions of the models too.

Here we discuss three relevant time-dependent FEM models, i.e. those describing the erosion kinetics. (Wang et al., 2014) modeled pipe progression using a 2D FEM model with steady seepage flow, turbulent pipe flow and a primary erosion criterion. Progression is determined by a critical pore shear stress at the tip (Fujisawa et al., 2010) and the rate of progression by an erosion coefficient depending on excess pore shear stress. Secondary erosion (pipe enlargement) and flow resistance due to the eroded sediment is not included. The direction of progression is free. The model is validated on $H_c$ in one test; the time-dependent

---

[*] Corresponding author at: Department of Hydraulic Engineering, Delft University of Technology, Stevinweg 1, 2628 CN Delft, The Netherlands.
*E-mail address:* pol@hkv.nl (J.C. Pol).

https://doi.org/10.1016/j.compgeo.2024.106068
Received 13 April 2023; Received in revised form 21 December 2023; Accepted 2 January 2024

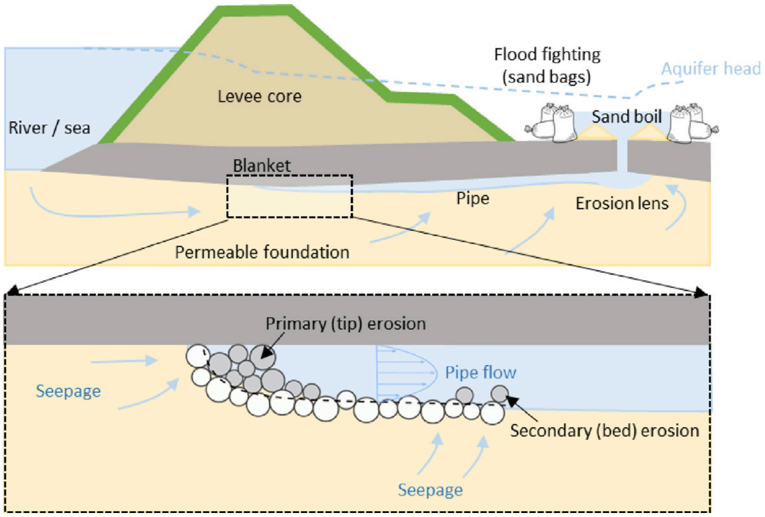

**Fig. 1.** Visualization of the main processes of backward erosion piping.

development is not validated. Rotunno et al. (2019) used a multi-phase model with 3D transient seepage flow, turbulent pipe flow, and both a primary and secondary erosion criterion. Primary erosion is modeled using the approach in Fujisawa et al. (2010), secondary erosion by a critical Shields parameter and empirical excess shear stress relation. Eroded sediment is transported as fluidized sand. The model is calibrated on two large-scale experiments, including one with data on time-dependent development, and was applied to the same large-scale experiment as used in the present paper (Callari and Pol, 2022). Wewer et al. (2021) modeled the time-dependent pipe progression in a 2D transient seepage model, where the pipe is represented by an increased permeability and the erosion rate at the exit is prescribed by laminar sediment transport equations. Using an assumption for the relation between pipe length and pipe depth, the erosion rate is translated to a pipe progression rate. The model is validated on a large-scale experiment. An advantage of the approach is the limited computational time and the explicit modeling of laminar sediment transport. Limitations are the 2D approach and the required assumption for the pipe depth as function of length.

This article describes an extension of the 3D finite element model (FEM) by van Esch et al. (2013) to simulate the time-dependent development of BEP. Informed by recent observations of the erosion process (Pol et al., 2022), the novel description of the pipe lengthening and enlargement over time is based on a sediment mass balance and an empirical sediment transport relation for laminar flow. The model includes primary and secondary erosion and assumes laminar pipe flow modeled by an increased permeability. To the best of our knowledge, such an implementation of pipe progression and laminar sediment transport in a 3D seepage model is not available in the literature. Secondly, small- and large-scale experiments are modeled. Unlike the experiments used for previous modeling studies (Wang et al., 2014; Rotunno et al., 2019; Wewer et al., 2021), these experiments have a circular exit with strong flow concentration as mostly found in field conditions, so the groundwater flow is highly 3-dimensional. This comparison with experiments identified important challenges with 3D modeling of backward erosion on large scales. Finally, effects of grain size, scale, and overloading on the modeled pipe progression rate are analyzed, providing novel insights in the effect of these parameters.

## 2. Modeling approach

The basis for the developed numerical model is the DgFlow finite element model (van Esch et al., 2013; van Esch, 2014), which was developed to simulate backward erosion piping in 2D and 3D soil domains. The 2D-version of the model with a user interface (D-GeoFlow) is also being used in levee safety analyses in the Netherlands. DgFlow was initially based on secondary (bed) erosion, later primary (tip) erosion was incorporated as well (van Esch, 2015; Van Beek et al., 2022). DgFlow is an equilibrium model: for a given head difference it computes whether grain equilibrium can be satisfied and what the corresponding pipe dimensions are, but it does not model how that equilibrium state is reached in time. So the model can compute the critical head for BEP but not the time-dependent development. This time-dependent erosion is added in this article.

Section 2.1 summarizes the most important features of the current DgFlow model; for further details we refer to van Esch et al. (2013) and van Esch (2015). Section 2.2 discusses different potential modeling approaches to extend the model with time-dependent erosion, and Section 2.3 describes the approach chosen in this article for the time-dependent modeling of piping.

### 2.1. Current DgFlow finite element model

The DgFlow model couples 3-dimensional transient seepage flow, steady 1-dimensional laminar pipe flow and a grain stability criterion to simulate the development of the pipe length for an imposed head difference.

The pore water pressure $p$ in space $x$ and time $t$ is computed with transient groundwater flow equations considering mass conservation and Darcy's law:

$$(\alpha + n\beta)S\frac{\partial p}{\partial t} + n\frac{\mathrm{d}S}{\mathrm{d}p}\frac{\partial p}{\partial t} + \frac{\partial q_i}{\partial x_i} = 0, \quad q_i = -\frac{k_r\kappa_{ij}}{\mu}\left(\frac{\partial p}{\partial x_j} - \rho_w g_j\right) \tag{1}$$

where $\alpha$ [m$^2$/N] is the compressibility of the soil skeleton, $\beta$ [m$^2$/N] the compressibility of the pore water, $n$ [–] porosity and $S$ [–] the degree of saturation. Specific discharge $q_i$ [m/s] relates to relative permeability $k_r$ [–], intrinsic permeability $\kappa_{ij}$ [m$^2$], $\mu$ dynamic viscosity [N/m$^2$s] and density $\rho$ [kg/m$^3$]. The groundwater flow simulations in this article are simplified to quasi-steady saturated flow ($\alpha = 0$, $\beta = 0$, $k_r = 1$, $S = 1$) because the groundwater flow in the experiments responds relatively fast compared to the time scale of erosion.

Pipe flow is based on laminar Poiseuille flow between parallel plates ($w \gg a$), which provides the relation between pipe discharge, depth and hydraulic gradient:

$$\frac{\mathrm{d}p}{\mathrm{d}x}a^3 w = 12 U w a \mu \tag{2}$$

in which $a$ denotes pipe depth [m], $w$ pipe width [m], $p$ pore pressure [N/m$^2$], $U$ cross-sectional average flow velocity [m/s] and $x$ horizontal distance [m]. In DgFlow, $w$ is related to $a$ using a specified $w/a$ ratio. The acting bed shear stress $\tau_{bed}$ for parallel plates is given by:

$$\tau = R\frac{\mathrm{d}p}{\mathrm{d}x} = \frac{a}{2}\frac{\mathrm{d}p}{\mathrm{d}x} \tag{3}$$

in which $R$ is the hydraulic radius [m]. The grain stability is modeled following White (1940) and Sellmeijer (1988) in which the critical bed shear stress is given by:

$$\tau_c = \eta\frac{\pi}{6}(\rho_s - \rho_w)gd\tan(\theta) \tag{4}$$

in which $\eta$ is White's coefficient [–], $\rho_s$ sediment density [kg/m$^3$], $d$ grain size [m] and $\theta$ bedding angle [deg]. Equating Eqs. (3) and (4) yields the pipe equilibrium condition. Based on experimental data, Van Beek (2015) proposed to use $d = d_{50}$, $\eta = 0.3$ and $\theta = -8.125 \cdot \ln(d_{50}) - 38.777$. This is also known as the Calibrated White approach.

The Poiseuille pipe flow and Darcy groundwater flow equations have a similar form: in both cases the discharge is proportional to the pressure gradient. Therefore, the pipe flow can be solved as part of the groundwater computation, using an equivalent permeability $\kappa_p$ which corresponds to a rectangular pipe with depth $a$ and width $w$. For 1D pipe elements in a 3D model, this relation becomes (van Esch, 2015):

$$\kappa_p = \frac{wa^3}{12} \tag{5}$$

Note that $\kappa_p$ [m$^4$] is not equal to the intrinsic permeability of the soil $\kappa$ [m$^2$].

In a given time step, the equilibrium depth of all pipe elements is solved iteratively by step-wise increasing $a$ (and hence $w$ and $\kappa_p$) and updating the groundwater flow accordingly, until the equilibrium condition is met. The depth iteration step is given by $\Delta a = 100d/(\mathrm{mPicard}-1)$, where mPicard is a numerical model setting. See Fig. 1 in van Esch et al. (2013) for a graphical explanation of this iterative scheme. The pipe length increases if the primary erosion criterion is exceeded. The strength criterion for primary erosion is defined in terms of critical local hydraulic gradient over the first element upstream of the pipe tip $i_{tip,c}$ (van Esch, 2015; Rosenbrand et al., 2021; Robbins and Griffiths, 2021):

$$i_{tip} = \rho_w g\frac{\mathrm{d}p}{\mathrm{d}x} > i_{tip,c} \tag{6}$$

It is noted that this criterion depends on the mesh size, and $i_{tip,c}$ must be chosen such that it fits the mesh size.

Although the groundwater flow can be modeled as transient in DgFlow, the increase in pipe depth and length in response to that flow is instantaneous. The following sections present the proposed method to extend the current model with a time-dependent development of the pipe.

### 2.2. Approaches for time-dependent piping erosion modeling

Based on observations in small-scale experiments (Pol et al., 2022), the pipe progression in poorly graded sand can be described as follows. The erosion mechanism at the tip can be described as micro-scale slope failures which occur rather sudden if the seepage flow forces at the tip exceed the resistance of the packed grains. The sand is detached in groups of grains, although also individual particle movement occurs. Part of the sand keeps moving; another part settles on the bed in front of the pipe tip and is gradually transported by the flow (secondary erosion). Pipe pressure measurements showed that the sediment load in the pipe results in a temporarily higher flow resistance (pressure drop) in the pipe. Consequently this gives temporarily a lower tip gradient which delays the pipe lengthening. When a sufficient amount of sand is transported so that the tip gradient has recovered to its critical value, the next slope failure occurs. These observations indicate that the sediment transport capacity of the pipe is an important driving factor in the progression rate.

This dynamic process can be modeled using different approaches which represent the dynamics of the erosion process with different levels of detail:

(1) The first method is to solve a sediment mass balance in space and time with a sufficiently small time step to capture the dynamics of the sediment movement in the pipe. This could simulate the above-mentioned temporary increase and decrease in flow resistance due to sediment moving through the pipe, either represented as a lower depth or a higher sediment concentration. The sediment from the collapsing tip element is added as a source term to the upstream pipe element once the primary erosion criterion is exceeded (Rotunno et al., 2019). This approach reflects the above-mentioned observations well. However, a major drawback is the small time step needed to simulate the dynamic sediment wave propagation through the pipe.

(2) The second method is to solve the sediment balance in space and time as well, but the tip element is gradually deepened by the same secondary erosion laws as the rest of the pipe, instead of an instantaneous sediment mass transfer from soil to the pipe. Here the progression rate is still driven by the sediment transport capacity, but the dynamics of the moving sediment wave are not solved. This allows for larger time steps and hence more efficient simulations. To our best knowledge, this approach has not been used yet.

(3) A third method is to solve the sediment balance in time, but integrated over the pipe length (Wewer et al., 2021). Here the increase in pipe volume equals the sediment transport capacity at the downstream end, and the spatial distribution of the erosion (lengthening and deepening) is forced by an assumed relation between pipe depth and pipe length. As this approach also does not simulate the dynamics of sediment movement and multiple soil elements can switch to pipe elements within a time step, the time step can be relatively large. However, this approach is not compatible with the current model approach of DgFlow in which each pipe element is deepened based on the local acting and critical shear stresses.

To keep the simulation time step relatively large and to avoid any assumption of a pipe depth profile, we adopt the second method as explained further in Section 2.3.

### 2.3. Model extension with time-dependent erosion

We extend the current 3D DgFlow model (van Esch, 2015) with a time-dependent formulation of the backward erosion process. First, we describe here the main features of the employed method, which is based on the second approach in the previous section. As DgFlow is an equilibrium model, it computes the pipe depth at which the pipe bed is in equilibrium ($\tau = \tau_c$). Based on the experiments in Pol et al. (2022), we assume that the rate of pipe progression ($\mathrm{d}l/\mathrm{d}t$) depends on the sediment transport capacity of the pipe flow, which is a function of the degree to which the critical shear stress is exceeded ($\tau - \tau_c$). To model this time-dependent process in DgFlow, we compute the pipe depth increase based on a sediment mass balance and sediment transport equations for laminar flow. In this way, the computed pipe depth can be temporarily smaller than the equilibrium depth that is computed using the current DgFlow model. The lower the shear stress, the more time it takes to reach the equilibrium depth. This pipe deepening (secondary erosion) affects the hydraulic gradient at the pipe tip, and therefore the time until the tip gradient exceeds its critical value and the pipe length increases (primary erosion). So, secondary erosion is the driving factor.

#### 2.3.1. Secondary erosion

Pipe deepening by secondary erosion is governed by a sediment balance (Fig. 2). The sediment balance of an element i with fixed length $\Delta x_i$ but variable depth $a$ and width $w$, subject to a volumetric sediment transport rate $Q_s$ [m$^3$/s] over the time interval $\Delta t$ is given by:

$$a_{t,i}w_{t,i}\Delta x_i = a_{t-\Delta t,i}w_{t-\Delta t,i}\Delta x_i + \frac{(Q_{s,out} - Q_{s,in})\Delta t}{(1-n)} \tag{7}$$

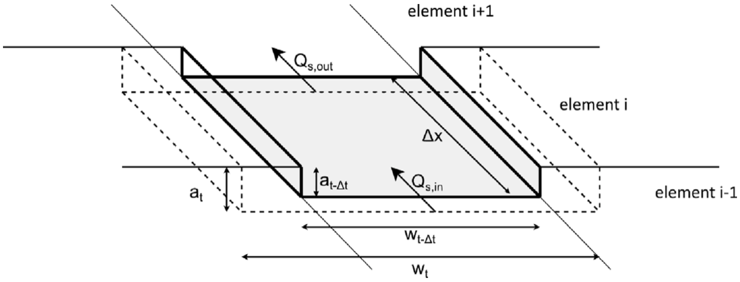

**Fig. 2.** Sediment balance of an element: increase in pipe volume (depth $a$, width $w$) equals change in sediment transport capacity ($Q_{s,out} - Q_{s,in}$).

This can be written in terms of the volumetric sediment transport rate per unit width $q_v$ [m$^2$/s] as:

$$a_{t,i}w_{t,i}\Delta x_i = a_{t-\Delta t,i}w_{t-\Delta t,i}\Delta x_i + \frac{(q_{v,t-\Delta t,i}w_{t-\Delta t,i} - q_{v,t-\Delta t,i-1}w_{t-\Delta t,i-1})\Delta t}{(1-n)} \tag{8}$$

This balance is similar to the Exner equation which is widely used for sediment transport in rivers:

$$(1-n)\frac{\partial aw}{\partial t} = \frac{\partial q_v w}{\partial x} \tag{9}$$

Assuming a fixed depth-width ratio $N$ and only an increase in depth, substitution of $w = N \cdot a$ into Eq. (8) and division by $N \cdot \Delta x$ gives:

$$a_{t,i}^2 = a_{t-\Delta t,i}^2 + \frac{\langle q_{v,t-\Delta t,i}a_{t-\Delta t,i} - q_{v,t-\Delta t,i-1}a_{t-\Delta t,i-1}\rangle \Delta t}{(1-n)\Delta x_i} \tag{10}$$

Here $\langle . \rangle$ denotes the positive part (only depth increase). Preventing the model to simulate a decrease in pipe depth may introduce an error in the sediment balance in case $\mathrm{d}q_v/\mathrm{d}x < 0$. However, we motivate this choice by the fact the pipe flow rate always increases with distance from the pipe tip. Eq. (10) is used to compute the pipe depth in each pipe element based on the pipe depth in the previous time step and sediment transport rate in the current and upstream elements in the previous time step. The computed sediment flux $q_v$ [m$^3$/s/m] is based on an empirical relation with the excess bed shear stress in laminar flows:

$$q_v = C_{e,\tau} \cdot \tau\langle \tau - \tau_c \rangle \tag{11}$$

Other excess shear stress equations have been considered, but this form is simple and matches well with laminar flow experiments in rectangular flumes (Pol et al., 2022). The factor $C_{e,\tau}$ [m$^2$ Pa$^{-2}$ s$^{-1}$] is a model parameter, the acting bed shear stress is based on parallel plates (Eq. (3)) and the critical bed shear stress is determined with Eq. (4). $C_{e,\tau}$ is in fact the combination of two scaling terms and an empirical coefficient, because Eq. (11) was originally written in dimensionless form as Pol et al. (2022):

$$\frac{q_v}{(\rho_s - \rho_w)gd^3/\mu} = C_e \cdot \Theta\langle \Theta - \Theta_c \rangle \tag{12}$$

where $\Theta = \tau/(\rho_s - \rho_w)gd$ is the Shields number and $C_e = 0.08$ is an empirical dimensionless coefficient. In Eq. (12) there is a sediment transport scaling term $C_1 = (\rho_s - \rho_w)gd^3/\mu$ and a scaling term $C_2 = 1/(\rho_s - \rho_w)gd$ which is the scaling between shear stress and Shields number. So $C_{e,\tau}$ can be written as:

$$C_{e,\tau} = C_e C_1 (C_2)^2 = \frac{C_e d}{(\rho_s - \rho_w)g\mu} \ [\mathrm{m}^2\ \mathrm{Pa}^{-2}\ \mathrm{s}^{-1}] \tag{13}$$

The empirical regression coefficient $C_e = 0.08$ was derived using $d_{50}$ (Pol et al., 2022), hence the $d_{50}$ should be used as representative diameter in this formula. So, the pipe deepening (secondary erosion) is controlled by Eqs. (10), (11), (3) and (4).

### 2.3.2. Primary erosion

In the current DgFlow model, pipe lengthening (primary erosion) is controlled by the following criterion (van Esch, 2015; Rosenbrand et al., 2021): the first soil element upstream of the pipe switches to a pipe element if the local hydraulic gradient over that soil element exceeds a critical value $i_{tip,c}$ (Eq. (6)). Upon opening, a pipe element gets an initial depth $a_{ini}$ to avoid an unrealistically low equivalent permeability $\kappa_p$ and corresponding high hydraulic gradient which could stop the pipe from further progression. $a_{ini}$ is a model parameter, and typically chosen in the order of $d_{50}$. In our time-dependent model, this initial volume ($a_{ini}^2 \cdot N$) is created instantaneously and not part of the sediment balance, and therefore introduces an error in the rate of pipe deepening. When the pipe depth is much larger than $a_{ini}$, this error is small.

Note that the model includes no explicit time-dependency in the primary erosion rate, unlike for instance Fujisawa et al. (2010) or Rotunno et al. (2019) who employ also a transport law for primary erosion. Instead, in our approach the primary erosion of an element occurs instantaneously but the rate of progression is limited by the sediment transport rate in the pipe. A low transport rate results in slowly increasing pipe depths, which lead to higher flow resistance and therefore indirectly controls the rate of primary erosion. This approach can be justified if the primary erosion occurs in relative short timescales, for instance in poorly graded sands which are often present beneath river levees.

### 2.3.3. Integration in DgFlow simulation procedure

The flow chart of Fig. 3 shows the DgFlow model simulation procedure; the additions for time-dependent erosion described in this paper are marked red. First the groundwater flow is solved without a pipe to obtain hydraulic gradients in the entire domain. Then, in each time step, the model performs two main computations as indicated by the shaded boxes: a secondary erosion procedure and a primary erosion check. In the secondary erosion procedure, the depth $a$ of all open pipe elements is increased incrementally by $\Delta a$ until the equilibrium depth is found ($\tau = \tau_c$) or the maximum depth that can be reached by the current sediment transport rate ($a_{max}$). The effect of the increasing depth on the groundwater flow is incorporated using the equivalent permeability $\kappa_p$. Then the shear stress $\tau$, sediment transport rate $q_v$ and maximum depth $a_{max}$ are updated accordingly based on the hydraulic gradients from the groundwater flow solution. When the pipe depth has been determined for all open pipe elements, the primary erosion criterion is checked at the first element upstream of the pipe. If the critical gradient is exceeded, that element switches to a pipe element with initial depth $a_{ini}$ and the secondary erosion procedure is repeated. Otherwise, the computation is repeated for the next time step with corresponding head boundaries. The added formulations for time-dependence are indicated in red. The pipe depth may only increase up to the depth $a_{max}$ which follows from Eqs. (10) and (11) instead of increasing to the equilibrium depth governed by $\tau = \tau_c$. Furthermore, a threshold depth $a_{th}$ was added for primary erosion to be able to include an additional delay, but in all computations we use $a_{th} = a_{ini}$ so this extra criterion has no effect.

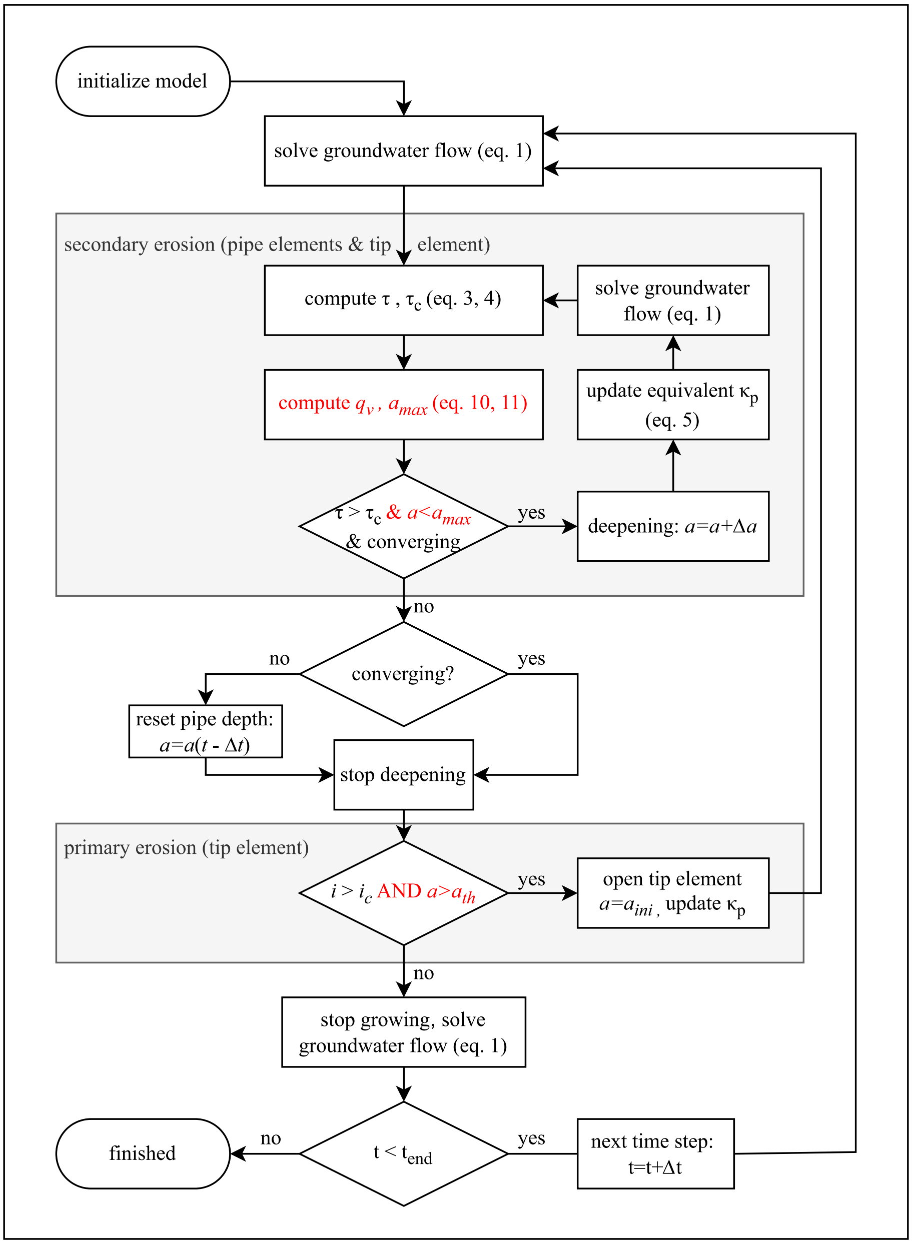

**Fig. 3.** Flow chart of the DgFlow simulation including the extension for time-dependent erosion in red.

### 2.3.4. Step sizes

Relevant numerical step sizes related to the secondary erosion are pipe grid size $\Delta x$, time step $\Delta t$ and depth increment $\Delta a$.

To avoid the progression rate to depend directly on the time step or grid size, opening of an element should take multiple time steps. In that way, the depth of the first pipe element can increase gradually. This requires that $\Delta x/\Delta t \gg \mathrm{d}l/\mathrm{d}t$. So for a given pipe element size, the maximum time step can be estimated if the order of magnitude of the progression rate is known.

Secondly, the depth iteration step $\Delta a$ must be smaller than the depth increase during one time step ($\Delta a/\Delta t < \mathrm{d}a/\mathrm{d}t$). The reason is that when the sediment transport becomes too low, so that $da < \Delta a$, the pipe depth will not increase anymore. $\Delta a$ is controlled by the numerical model parameter mPicard and the grain size $d$ (see Section 2.1). As the smallest amount of pipe deepening that must be simulated is difficult to estimate beforehand, one can evaluate the sensitivity of the model results for mPicard. For the small-scale simulations in which $\Delta t = 10$ s (Section 3), mPicard = 2000 was found sufficiently stable.

## 3. Simulation of experiments

### 3.1. Method

In order to test the developed model, several small-scale (Pol et al., 2022) and large-scale (Pol et al., 2021) experiments are simulated. We used selected small-scale experiments from Pol et al. (2022) as these contain densely spaced pore pressure measurements as well as the pipe length development over time. For two sand types (B25 and FS35), we selected experiments with dense and loose sand and one with overloading ($H > H_c$). This resulted in the following six tests: B25-232 (dense), B25-245 (loose), B25-248 (dense, 20% overloading), FS35-238 (dense), FS35-240 (loose) and FS35-242 (dense, 20% overloading). Additionally, the large-scale experiment in Pol et al. (2021) is simulated. Material parameters and other model inputs are shown in Table 1 and further explained in the following sections.

Due to the standard experimental procedure, the applied head is only slightly above the critical head. Hence, the simulated pipe development with the applied head as boundary would be highly sensitive to

**Table 1**
Model input and calibrated parameters used for simulation of experiments.

| | | Small-scale | | | | | | Large-scale |
|---|---|---|---|---|---|---|---|---|
| | | B25-232 | B25-245 | B25-248 | FS35-238 | FS35-240 | FS35-242 | FPH |
| Input parameters | | | | | | | | |
| $d_{50}$ | mm | 0.228 | 0.228 | 0.228 | 0.422 | 0.422 | 0.422 | 0.185 |
| $\rho_s$ | kg/m$^3$ | 2650 | 2650 | 2650 | 2650 | 2650 | 2650 | 2610 |
| $\rho_w$ | kg/m$^3$ | 1000 | 1000 | 1000 | 1000 | 1000 | 1000 | 1000 |
| $\kappa$ | $10^{-11}$m$^2$ | 2.75 | 3.16 | 2.55 | 10.2 | 12.2 | 8.87 | 1.2 |
| $n$ | – | 0.377 | 0.402 | 0.377 | 0.381 | 0.399 | 0.377 | 0.383 |
| $\theta$ | ° | 29.36 | 29.36 | 29.36 | 24.36 | 24.36 | 24.36 | 31.06 |
| $\mu$ | Pa s | 0.001 | 0.001 | 0.001 | 0.001 | 0.001 | 0.001 | 0.00133 |
| $\eta$ | – | | | | | | | 0.4 |
| $i_{tip,c}$ (5 cm) | – | | | | | | | 1.1 |
| Calibrated | | | | | | | | |
| $\eta$ | – | 0.35 | 0.3 | [a] | 0.35 | 0.3 | [a] | [b] |
| $i_{tip,c}$ (1 cm) | – | 1.1 | 0.9 | [a] | 1.1 | 0.9 | [a] | [b] |
| $w/a$ | – | 20 | 25 | [a] | 25 | 25 | [a] | 700 |
| $C_e$ | – | 0.012 | 0.010 | 0.030 | 0.018 | 0.007 | 0.018 | 0.014 |

[a] Not available in overloading experiments.

[b] Not calibrated but estimated based on measurements.

the critical head being simulated accurately. Therefore, the calibration was done in two steps. First, parameters $\eta$, $w/a$ and $i_{tip,c}$ were calibrated to resemble the critical conditions, i.e. the conditions during the time step in which the critical head ($H_c$) is reached. Then, $C_e$ was calibrated to resemble the pipe length development over time, using the calibrated values for $\eta$, $w/a$ and $i_{tip,c}$.

Four goodness of fit criteria are used for the critical conditions: (1) the relative error in the critical head, (2) the relative error in the critical pipe length, (3) the RMSE of the head profile along the entire center axis and (4) the RMSE of the head profile in the pipe. Simulations with different combinations of calibration parameters are ranked on each criterion, and the product of these four ranks determines the total rank. The total rank is minimized, so the four criteria are equally important in the calibration. For the pipe length development over time, two goodness of fit criteria are used: (1) the RMSE of total pipe length development $l(t)$ and (2) the relative error of the average progression rate in the progressive phase. Again simulations with different parameter combinations are ranked on each criterion, and the product of these two ranks determines the total rank, which is minimized.

### 3.1.1. Small-scale experiments

For the small-scale tests, four parameters ($\eta$, $w/a$, $i_{tip,c}$) are calibrated to resemble the critical head, although these variables were also measured. The erosion coefficient $C_e$ is calibrated to resemble the pipe length development over time. The two small-scale overloading experiments are only used for the calibration of $C_e$, because equilibrium was not reached in these experiments.

The computational grid has 1D linear pipe elements with $\Delta x = 0.01$ and tetrahedral soil elements of 0.02 m (Fig. 4(a)). Boundary conditions are located on the surfaces as indicated in Fig. 4(b). These are head boundaries based on the measured head difference over the sample, corrected for head loss in the upstream filter and the exit hole. Other boundaries are no-flow. The time step $\Delta t = 10$ s is chosen based on the expected progression rate ($10^{-4} - 10^{-3}$ m/s) and grid size.

### 3.1.2. Large-scale experiment

For the simulation of the large scale experiment, only $w/a$ and $C_e$ are calibrated because the head measurement spacing (80 cm) is not sufficient to calibrate more parameters on the critical head profile. $w/a$ was chosen because no pipe geometry measurements are available for this experiment. A value $\eta = 0.4$ is chosen based on critical shear stress measured on this sand Pol et al. (2022) and $i_{tip,c}$ is chosen as 1.1. This value follows from the measured critical gradient of 0.28 over 80 cm spacing in the large-scale experiment (Pol et al., 2021), which is translated to an average gradient over 5 cm. This was done using the critical secant gradient function from Robbins (2022), which can be rewritten as:

$$i_c(\Delta x) = i_0 \sqrt{\frac{\Delta x_0}{\Delta x}} \tag{14}$$

where $i_0$ is the measured gradient, $\Delta x_0$ the measurement spacing and $\Delta x$ the desired spacing. The pipe grid size is 5 cm and the time step is 100 s. The boundary conditions are similar to the small-scale experiment, but the aquifer is larger and relatively long and narrow.

## 3.2. Results

### 3.2.1. Small-scale experiments

The best-fit values for the calibrated parameters are given in Table 1. The obtained values for $\eta$ are close to the 0.3 found by Van Beek (2015) and the measured critical shear stresses in the small-scale experiments. The obtained $w/a$-ratios are also within the range of 10–30 measured in the experiments. These two parameters affect the hydraulic gradient in the pipe. The obtained critical tip gradients over the model grid spacing of $\Delta x = 1$ cm (0.9 for loose and 1.1 for dense sands) are translated to gradients over $\Delta x = 2$ cm using Eq. (14) as the measurement spacing was 2 cm. This yields gradients of 0.64 and 0.78 respectively. The measured $i_{tip,c}$ for the loose sand in Pol et al. (2022) was lower (range 0.4–0.6), but for the dense sand this was similar to the calibrated value (range 0.6–0.8). For 2 cm spacing, Xiao et al. (2019b) report measured values between 0.5 and 2. Robbins (2022) reports gradients of 0.5–1.1 for similar grain size, porosity and uniformity. Riha and Petrula (2023) report values of 1.2–1.8 for similar porosity, but they use less uniform sand which is expected to have a higher critical gradient (Robbins, 2022).

The calibrated values for $C_e$ are consistent between the two sands but approximately a factor 3 to 10 lower than the 0.08 expected from Eq. (13). This may be the partly caused by the representation of the pipe as a straight rectangular channel, which requires less transport to obtain a given pipe length compared to a meandering channel. Furthermore, it is noted that sediment transport rates are typically associated with large uncertainties: variations of one order of magnitude are commonly observed in sediment transport relations based on lab tests.

Fig. 5 shows the best-fit result for test B25-245. The simulated head profile (Fig. 5(a)) and pipe length development (Fig. 5(c)) agree well with the measurements. Computed pipe flow conditions are shown in Fig. 5(b). The computed pipe depth of 1 mm is slightly larger than the measured 0.8 mm, and the flow is clearly laminar (Re≈20) (see Fig. 6).

### 3.2.2. Large-scale experiment

When using the same $w/a = 20$ as in the small-scale experiments, the critical head profile is strongly underestimated by the model (yellow line in Fig. 6(a)). Apparently, there is more resistance present than what is modeled with parameters based on the small-scale experiments. This can be something in the execution of the experiment, or a physical process which is not represented well in the model. Here we increased the $w/a$ ratio to match the measured head profile, although other model parameters could be adjusted (e.g. $\eta$).

A $w/a$ ratio of 700 was needed to obtain a reasonable head profile. As the $w/a$ ratio of 700 is far higher than found in small-scale tests, we simulated a few slightly different model configurations with more resistance to investigate how this changes the required $w/a$. First, the diameter of the circular downstream boundary was increased from 13 mm to 200 mm and 500 mm to simulate the influence of lens formation around the exit hole. Second, the soil permeability of $1.2 \cdot 10^{-11}$ m$^2$ was decreased to $6 \cdot 10^{-12}$ m$^2$, which is the expected value minus one standard deviation (lower bound). Third, a meandering pipe was implemented such that the actual pipe length was $\sqrt{2}$ times the straight pipe length of 7.2 m. This tortuosity can be around 1.5–2 in piping experiments (Wewer et al., 2021).

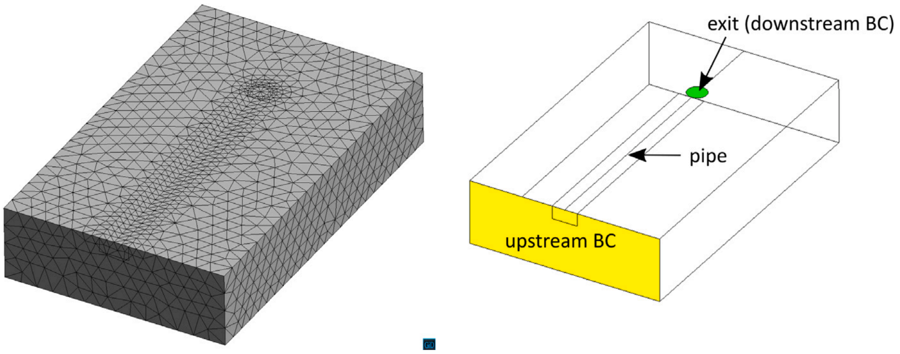

(a) Grid. (b) Boundary conditions.

**Fig. 4.** Small-scale model grid and head boundary conditions.

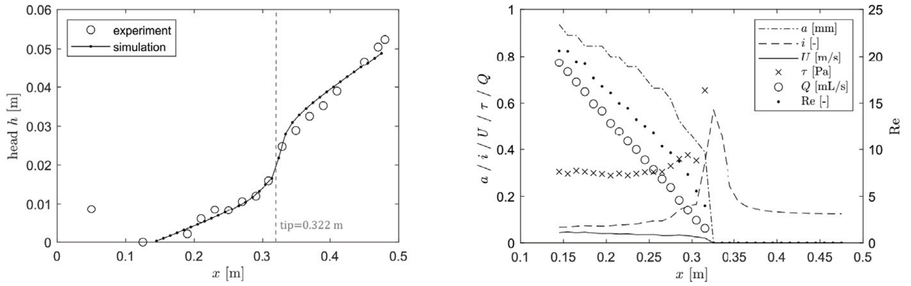

(a) Head profile in critical conditions. (b) Modeled pipe flow variables in critical conditions.

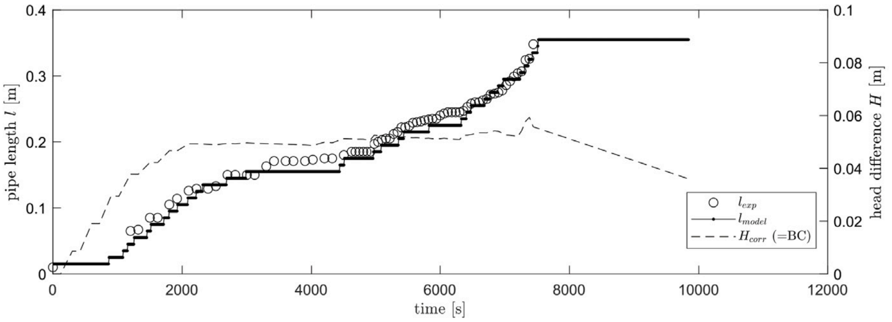

(c) Pipe length development and imposed head.

**Fig. 5.** Calibrated model results for small-scale experiment B25-245 ($i_{tip,c} = 0.9$, $\eta = 0.3$, $C_e = 0.014$).

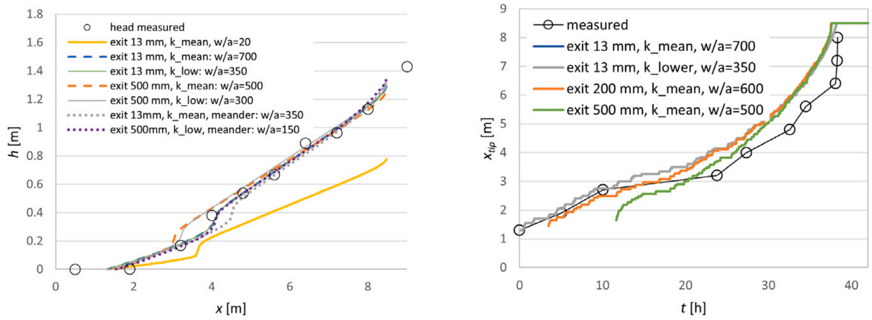

(a) Head profile in critical conditions. (b) Development of pipe tip position $x_{tip}$.

**Fig. 6.** Calibrated model results for the large-scale experiment ($i_{tip,c} = 1.1$, $\eta = 0.4$, $C_e = 0.014$) compared with measurements.

The required $w/a$ ratio decreases with all changes, but even in the lowest case with exit diameter of 500 mm, lower bound permeability and meandering pipe, a value of 150 is still required (Fig. 6(a)). Note that this value does not necessarily reflect the physical geometry of the pipe cross section, but through calibration it became a general pipe resistance factor. The source of this additional resistance is not entirely clear. Potential explanations include wider and shallower pipes, a leaky aquifer, or additional resistance due to pipe meandering, turbulence, upward seepage, clay cover roughness, or a reduced permeability due to accumulation of fines. Hence it remains also uncertain how this resistance depends on the scale of the experiment. Because the scale-dependence potentially has a large impact on model results on field scale, this needs further study. For instance by simulating multi-scale hole-type experiments that include information on pipe geometry and pipe flow conditions. It is noted that a recent study with the 3D DgFlow model without primary erosion also indicates that the critical head is underestimated (Van Beek et al., 2022), and that $w/a \approx 100$ is needed to reproduce medium scale laboratory experiments.

For the analysis of the pipe development over time, we calibrated $C_e$ for different scenarios of the permeability (expected and lower bound) and different exit diameters (Fig. 6(b)). The numerical simulations show a temporary decrease in progression rate around the critical length ($x_{tip} \approx 2.95$ m), which was also observed in the measurements. In all simulated cases, the obtained $C_e$ to match the measured total erosion time is close to 0.014. So similar to the small-scale experiments, the calibrated value is a factor 5–6 below that in Eq. (13), possibly due to the representation of the pipe as straight rectangular channel.

### *3.2.3. Concluding remarks*

The comparison with experiments shows that the DgFlow model with instantaneous erosion is well able to reproduce the measured critical head and critical pipe length in the small-scale tests with all calibrated parameters ($w/a$, $\eta$, $i_{tip,c}$) close to the measured ones. Only for the loose sand tests, the critical tip gradient found by calibration is slightly higher than measured. The critical conditions of the large-scale experiment could only be reproduced with a much higher pipe flow resistance than used for the small-scale experiments. Calibration of $w/a$ yields $w/a = 700$ compared to $w/a = 20$ in the small scale experiments. The reason for this additional resistance could not be fully demonstrated and needs to be studied in more depth.

With respect to the time-dependent pipe development, the modified DgFlow model can reproduce this reasonably well, although the erosion coefficient $C_e$ needs to be calibrated. Calibration on the different small-scale experiments yields $0.007 < C_e < 0.030$ (average: 0.016). Calibration of the large-scale experiment yields $C_e = 0.014$. It is a promising result that this is close to the average $C_e$ value from the small-scale experiments.

## 4. Effect of grain size, scale, and overloading

In Section 3, the developed model was tested and calibrated on several experiments. This section uses the model to study how factors such as grain size, scale and overloading affect the simulated pipe development.

### *4.1. Method: model setup*

To study the effect of grain size, scale, and overloading on the pipe development over time, we have set up a series of simulations in which those properties vary. In addition, the sensitivity of the computed development for several model assumption and parameters is investigated.

The simulations include six sand types as indicated in Table 2. Grain sizes range from 0.200–0.400 mm. For each grain size, two intrinsic permeabilities are used which correspond to a uniformity coefficient $C_u = d_{60}/d_{10}$ of 2 and 3 based on a correlation by Den Rooijen (1992). The bedding angle $\theta$ is based on Calibrated White (Van Beek, 2015). The erosion coefficient $C_e$ is assumed to be 0.08, the value in Eq. (13) prior to calibration, but varied in some cases to 0.008, 0.016 and 0.16 to investigate the sensitivity for $C_e$. Other parameters set as constant are: $\rho_s = 2650$ kg/m$^3$, $\rho_w = 1000$ kg/m$^3$, $\mu = 0.00133$ Pa s, $n = 0.4$, $\eta = 0.3$, $w/a = 20$, $a_{ini} = d_{50}$, $a_{thr} = d_{50}$.

**Table 2**
Sand characteristics used for simulation.

| Sand | $d_{50}$ [mm] | $C_u$ [–] | $\kappa$ [m$^2$] | $\theta$ [°] |
|---|---|---|---|---|
| S2-2 | 0.200 | 2 | $2.2 \cdot 10^{-11}$ | 30.4 |
| S2-3 | 0.200 | 3 | $9.7 \cdot 10^{-12}$ | 30.4 |
| S3-2 | 0.300 | 2 | $5.0 \cdot 10^{-11}$ | 27.1 |
| S3-3 | 0.300 | 3 | $2.2 \cdot 10^{-11}$ | 27.1 |
| S4-2 | 0.400 | 2 | $9.0 \cdot 10^{-11}$ | 24.8 |
| S4-3 | 0.400 | 3 | $3.9 \cdot 10^{-11}$ | 24.8 |

**Table 3**
Model settings and parameters used for simulation at different scales ($L$).

| $L$ [m] | Pipe mesh [m] | Soil mesh [m] | Time step [s] | $i_{tip,c}$ [–] |
|---|---|---|---|---|
| 0.9 | 0.02 | 0.05 | 10 | 0.7 |
| 3 | 0.02 | 0.2 | 10 | 0.7 |
| 9 | 0.1 | 0.5 | 200 | 0.2 |
| 30 | 0.1 | 2 | 200 | 0.2 |
| 90 | 0.2 | 5 | 500 | 0.15 |

Simulations were run at five scales ( Table 3), represented by the seepage length $L$ of 0.9, 3, 9, 30 and 90 m. The aquifer geometry is constant across scales: aquifer depth $D = L/3$, aquifer width $W = L$ and the distance between exit point and polder boundary equals $2 \cdot D$. The critical gradient for primary erosion $i_{tip,c}$ depends on sand properties (Robbins et al., 2017) and pipe grid size. As the pipe grid size increases with scale, the modeled value of $i_{tip,c}$ varies with scale. For the purpose of illustration, we assume that $i_{tip,c} = 0.7$ (for $\Delta x = 2$ cm). This value is based on the dense ($D_r = 0.8$) experiments in Pol et al. (2022). To obtain $i_{tip,c}$ for $\Delta x > 2$ cm, the critical head $H_c$ as calculated with the finest grid is reproduced using coarser grids by reducing $i_{tip,c}$. So the tip gradient over 5 cm is found by matching the critical head with the 2 cm pipe grid simulation. This is repeated with 5, 10 and 20 cm grids, and the resulting critical gradients are given in Table 3.

For each combination of scale and grain size, we first determine the critical head $H_c$ using a simulation with gradually increasing head difference and instantaneous erosion (very high $C_e$). Then, we run time-dependent simulations (normal $C_e$) with different degrees of overloading. The applied constant head drop $H(t)$ equals $1.05 \cdot H_c$, $1.1 \cdot H_c$, $1.2 \cdot H_c$, $1.3 \cdot H_c$ and $1.4 \cdot H_c$.

The model is similar to the one used for simulating the small-scale experiments (Fig. 4), but the vertical boundary at the polderside (downstream) is a constant head boundary with head equal to the exit point instead of a no-flow boundary. This is assumed to be a more realistic representation of field conditions. The soil and pipe grid sizes used for the analysis of the progression rates are indicated in Table 3, as well as the typical time step in these simulations.

So the main variations are: 5 scales ($L$), 6 sand types, 4 erosion coefficients ($C_e$) and 5 degrees of overloading ($H/H_c$). Not all 600 possible combinations have been simulated because of limitations in computational time, but a total of 74 (see Tables A.4–A.6 in Appendix). For instance, other sands than S2-2 and variations in $C_e$ were only simulated on the scales $L = 3$ and $L = 30$ m. The set of 74 includes 59 hole-exit simulations, 7 plane-exit simulations and 8 simulations for sensitivity analyses.

### *4.2. Results: critical conditions*

In general, the model behavior for equilibrium conditions (steady state: $C_e$ sufficiently high for an instantaneous response) are in qualitative agreement with previous experiments and model studies, which gives better confidence in the new, temporal behavior. This includes the difference between initiation and progression (Van Beek, 2015) as shown in equilibrium curves, and effects of grain size and scale on the critical head.

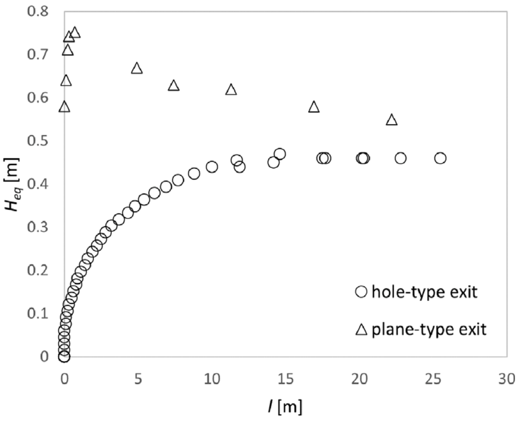

**Fig. 7.** Equilibrium curve: equilibrium head drop $H_{eq}$ as function of pipe length $l$. Results for S2-2 sand and $L = 30$ m modeled with adapted DgFlow model.

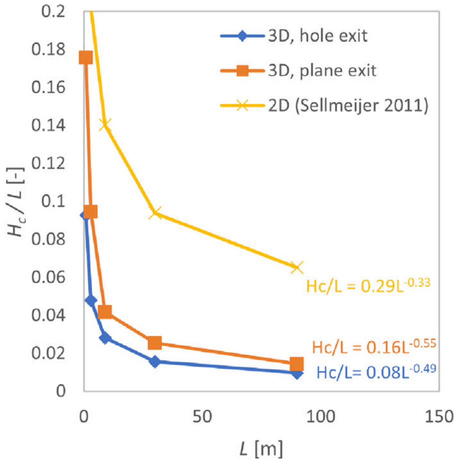

**Fig. 8.** Scale effect in modeled critical head difference $H_c$ ($d_{50} = 0.2$ mm, $w/a = 20$).

The equilibrium curve (Hanses, 1985) shows the equilibrium head $H_{eq}$ as function of pipe length. For 3D hole-type configurations, the modeled $H_{eq}$ initially increases with pipe length until the critical head $H_c$ is reached (Fig. 7), behavior also shown by Robbins and Griffiths (2021). After the critical point, $H_{eq}$ decreases only slightly. 3D plane-type configurations do not reach equilibrium once erosion starts (initiation-dominated) and $H_{eq}$ decreases steadily with pipe length.

The critical head $H_c$ is defined as the maximum of the equilibrium curve. Here we focus on the effect of scale, expressed in terms of the seepage length: $H_c/L \propto L^{\alpha}$. Fig. 8 shows that the critical gradient $H_c/L$ decreases with $L$, and we found that the exponent $\alpha$ depends on configuration (2D or 3D, hole or plane exit). The lower critical head in case of 3D flow towards a hole-type exit compared to a plane-type exit or the critical head predicted by the 2D Sellmeijer model confirms experimental findings by Vandenboer et al. (2018) and Van Beek (2015) An important finding is that the 3D simulations show a stronger scale effect: $\alpha \approx -1/2$ instead of $\alpha = -1/3$ as obtained for pipe progression in 2D (Sellmeijer, 1988). Hence extrapolation to larger scales in 3D yields even lower critical gradients. Scale effects in hole-exit experiments at different scales (Van Beek, 2015; Allan, 2018) indicate that $-0.45 < \alpha < -0.2$, weaker than the $\alpha \approx -1/2$ from the 3D model. Additional large-scale experiments or centrifuge experiments (Okamura et al., 2022) may provide more insights into the governing scale effects for hole-exit cases.

### 4.3. Results: pipe progression

The simulated head profile and pipe depth profile at different stages of the process under a constant head ($H/H_c = 1.1$) for a hole-type exit are shown in Fig. 9. Initially, the pipe is relatively shallow, which gives a high gradient in the pipe. When it gets longer, the pipe deepens gradually and the pipe gradient decreases. For larger pipe lengths, the deepening mainly takes place near the upstream end of the pipe. Here the inflow into the pipe is largest, which leads to the largest spatial gradient in sediment transport and hence most deepening. Fig. 10 shows the typical pipe length development over time under a constant head. In the initial erosion phase, the progression rate $\mathrm{d}l/\mathrm{d}t$ is highest. Later, it decreases to a fairly constant rate. When the pipe length approaches the seepage length, there is some acceleration, which appears most clearly on smaller scales and with little overloading.

#### 4.3.1. Average progression rates

The rest of this section focuses on the average progression rate in the part $L/2 < l < L$, which is approximately the progressive erosion phase ($l > l_c$). Three main factors of influence on the average progression rate are shown here: scale, grain size and degree of overloading. The results in Fig. 11 indicate that the progression rate increases with grain size and degree of overloading, and decreases with scale. Simulated pipe progression rates at field scale (90 m) are almost an order of magnitude slower than on the laboratory scale (0.9 m). The relative increase in progression rate with overloading is in line with experiments by Allan (2018) and Vandenboer et al. (2019). The influence of grain size and uniformity, for $L = 3 - 30$ m and at 10% overloading, is shown in Fig. 11(b). A higher $C_u$, and associated lower permeability, appears to have only limited effect on progression rates.

#### 4.3.2. Effect of local heterogeneity

To investigate potential effects of heterogeneity in the pipe path, we added a stronger sand barrier ($i_{tip,c} = 1.4$ instead of 0.7) in the pipe path at $2.8 < x < 3.2$ m for the simulation with S22 sand and $L = 3$ m. Fig. 12(a) shows that this increases the critical head from 0.14 to 0.18 m, but also increase the progression rate by a factor two once critical conditions are exceeded because the applied head is larger. Under the same applied head ($H = 0.20$ m), the progression rate is similar, although the rate reduces when progressing through the barrier (Fig. 12(b)). So a locally stronger sand layer gives a higher critical head, but once exceeded this corresponds to a more severe overloading situation and higher progression rate.

#### 4.3.3. Sensitivity for model assumptions

We investigated the sensitivity of the simulated average progression rate to several model assumptions, both physical (erosion coefficient, locally stronger layer) and numerical (time step).

The simulated progression rate relates linearly to the erosion coefficient $C_e$. Hence, uncertainties in $C_e$ can be easily translated in terms of progression rate. This relation was observed for the hole-exit cases with $L = 3$ m and 30 m, $d_{50} = 0.200$ mm and 0.400 mm, all at 10% overloading. Secondly, the influence of time step $\Delta t$ was checked for the case with $L = 3$ m, S2-2 sand and 10% overloading. For this case we find only a 2% increase in average progression rate when doubling the time step from $\Delta t = 5$ s to $\Delta t = 10$ s. Finally, the sediment balance was checked by comparing the simulated increase in pipe volume per unit time ($\mathrm{d}V/\mathrm{d}t$) with the total sediment transport at the exit ($Q_s$). The difference between these terms was typically in the order of 10%, and are related to the sources of errors as mentioned in Section 2.3.

### 4.4. Regression model

Numerical models are often impractical to apply directly in reliability analyses due to the significant computational time (several hours). Therefore, we developed a regression model for the instantaneous progression rate based on a selection of numerical simulations from Section 4. The selection includes four base cases: hole-type exit simulations with two sands (S22 and S42) and two seepage lengths (3 m and 30 m). Each one has a equilibrium curve $H_{eq}(l)$ and critical head.

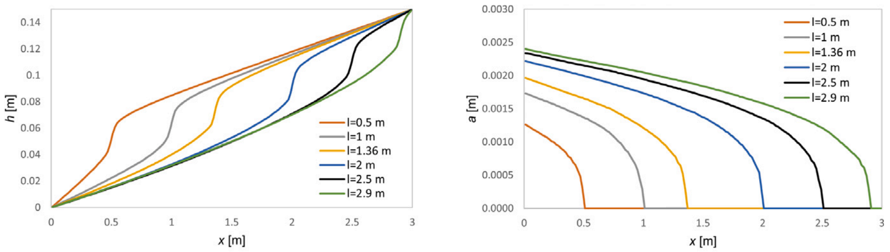

(a) Head profiles.

(b) Pipe depth profiles.

**Fig. 9.** Modeled head and depth profiles at different pipe lengths, for $L = 3$ m, S2-2 sand ($d_{50} = 0.200$ mm), $H = 0.157$ m. $l = 1.36$ m is the critical length.

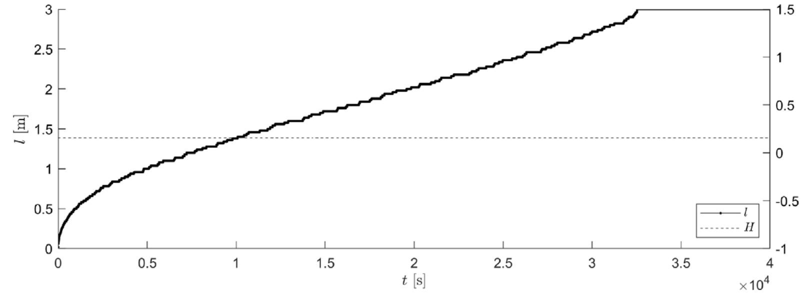

**Fig. 10.** Modeled pipe length development, for $L = 3$ m, S2-2 sand ($d_{50} = 0.200$ mm), $H = 0.157$ m, $H_c = 0.143$ m.

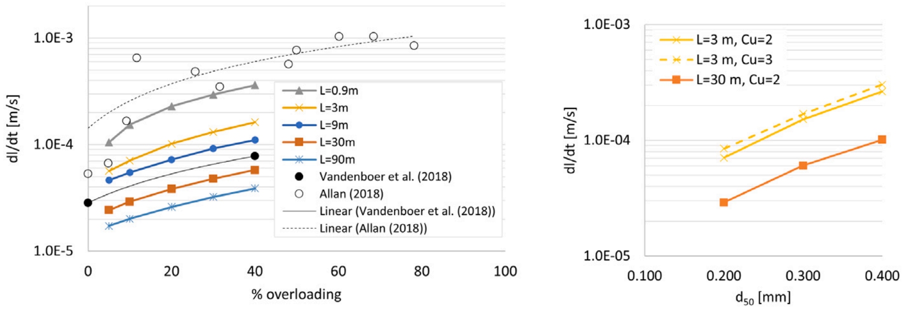

(a) Effect of scale and overloading for $d_{50} = 0.200$ mm. Allan (2018): $d_{50}$=0.3 mm, $L$=1.3 m. Vandenboer et al. (2019): $d_{50}$=0.155 mm, $L$=0.34 m.

(b) Effect of grain size and uniformity ($C_u$) for 10% overloading.

**Fig. 11.** Average progression rate for the pipe length interval $L/2 < l < L$.

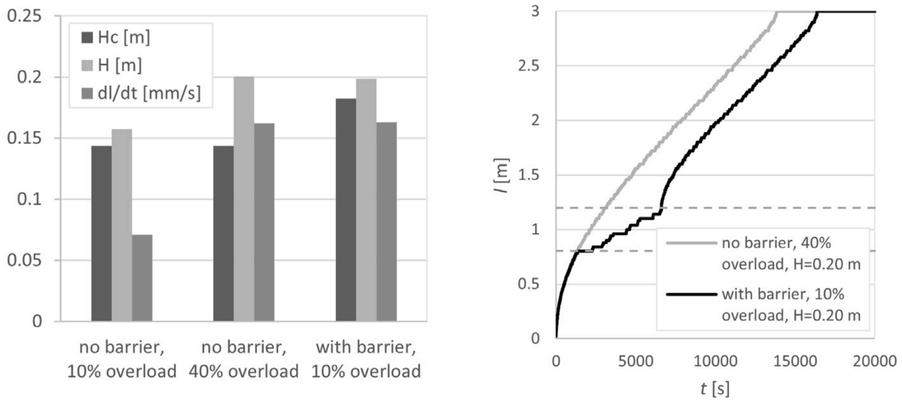

(a) Critical head $H_c$, imposed head $H$ and progression rate $dl/dt$.

(b) Pipe length development for $H = 0.20$ m. Dashed lines indicate position of barrier.

**Fig. 12.** Effect of locally stronger barrier on progression, for $d_{50} = 0.200$ mm and $L = 3$ m.

For each base case, simulations with different degrees of overloading and erosion coefficient $C_e$ are included to obtain variation in the rate of progression. A total of 31 simulations with 3100 data points are available, as the seepage length was divided in 100 equal segments to compute progression rates at different pipe lengths. 80% of this data is used for fitting, 20% for validation.

This resulted in the following regression function for the instantaneous progression rate $\frac{dl}{dt}(t)$ [m/s] as function of erosion coefficient $C_e$ [–], hydraulic conductivity $k$ [m/s] and degree of overloading $(H(t) - H_{eq})/L$ [–]:

$$\frac{dl}{dt}(t) = 89 \cdot C_e \left( k \frac{H(t) - H_{eq}(t)}{L} \right)^{0.81} \tag{15}$$

This equation is similar to Kézdi (1979), but extended with an overloading term and an exponent on the seepage velocity $R^2$ is 0.94. The equation can also be derived using $d_{50}$ instead of $k$, with similar performance. Additional simulations with varying combinations of $k$ and $d_{50}$ are needed to conclude which is a better predictor. Although fitted on hole-type exits, the order of magnitude for plane-type exits is also captured. For a more extensive discussion we refer to Pol (2022).

## 5. Discussion

This discussion focuses on three aspects of the numerical model: (1) the model's advancements compared to current engineering models, (2) model limitations, and (3) differences between the model and field conditions.

For the comparison with engineering models, we focus here on the model by Sellmeijer et al. (2011) which is used in routine safety assessments and design of levees in the Netherlands. The FEM implementation in DgFlow provides much more freedom in analyzing deviating aquifer characteristics, groundwater boundary conditions, and in particular the step to a 3D domain. Furthermore, the model of Sellmeijer et al. (2011) does not include a primary erosion criterion and the critical bed shear stress $\tau_c$ from White (1940) was modified in the 2011 re-calibration with small-scale experiments. In the FEM model we used an improved $\tau_c$ formulation by Van Beek (2015) which corresponds better to experiments. Finally, the main advancement of this work is the time-dependent secondary erosion formulation which allows to simulation the rate of pipe progression.

A first limitation of the model is that the pipe is represented as a straight rectangular channel, while lens formation, channel shape and channel meandering will affect both the predicted critical head and the progression rate. Secondly, the numerical formulation introduces two errors in the sediment balance (Section 2.3). These errors are limited but can be reduced by an improved numerical implementation. Finally, a general limitation of any BEP model is the uncertainty around the translation from small to large scales and the lack of multi-scale experiments with detailed measurements of the pipe flow and geometry. The importance of these scale effects is illustrated by the difference in scale effect between 2D and 3D simulations (Fig. 8), and the fact that prediction of $H_c$ for the large-scale experiment proved difficult when using the a priori estimate of $w/a = 20$ (Fig. 6(a)). The very low critical head that is obtained with the 3D model for field scale situations (Fig. 8) seems unrealistic based on the past performance of levees. Therefore, this modeled scale effect requires further analysis, in particular into the effect of using 1D line elements to model the pipe (Robbins et al., 2022) combined with the element size on different scales, and also into missing processes such upward seepage effects (Xiao et al., 2023) and turbulence effects in case of coarse sand and field scales (Hoffmans, 2022). Additionally, the effect of element type on the progression rate should be investigated.

Field conditions can deviate in several aspects from the simulations performed here, and hence result in different behavior. For instance, soil heterogeneity causes pipes to meander and form multiple branches when searching for the weakest path (Kanning, 2012; Robbins and Griffiths, 2018). This has different effects on the rate of pipe progression. Meandering pipes result in more head drop in the pipe (Wewer et al., 2021). Furthermore, the development of multiple or meandering pipe branches requires more sediment to be transported which will reduce the progression rate. On the other hand, a locally higher erosion resistance along the pipe path may result in a higher progression rate once this local barrier is exceeded (similar to overloading). In a broader sense, there is a limited understanding of 3D aspects of the BEP process in the field, as well as reliable field experiments. This makes it challenging to perform realistic BEP failure analyses.

## 6. Conclusions

This article develops a numerical model to simulate time-dependent development of backward erosion piping in a 3-dimensional domain. This model is based on the DgFlow numerical equilibrium model (van Esch et al., 2013; van Esch, 2015). We added a sediment transport formulation for secondary erosion (pipe deepening and widening), instead of the search for an equilibrium depth as in van Esch et al. (2013). In this way, the time required for pipe deepening limits the rate of pipe progression, and hence introduces the time-dependence in the backward erosion process. First, the model was tested on small-scale and large-scale experiments. Second, in a parametric study a variety of situations were simulated to explore how the critical head and pipe progression rate depends on grain size, scale and degree of overloading.

With respect to the predicted critical head, we draw the following conclusions. In the small-scale experiments, the model can reproduce the critical head profile including critical pipe length reasonably well, which gives confidence in the model performance on this scale. In the large-scale experiment, the input parameter $w/a$ (pipe width to depth ratio) could not be measured. Using $w/a = 20$ (as measured on small scale), the critical head of the large-scale test is significantly underpredicted. A much higher flow resistance in the pipe is required to reproduce the measured critical head profile. Although we identified potential causes of this difference (meandering, lens formation, lower permeability), a full explanation is still lacking, and further study is required due to its implications for predicting BEP on larger scales.

An important question for practical application is the scale effect: how does the critical gradient $H_c/L$ depend on scale, for instance the seepage length $L$. According to the 2D analysis by Sellmeijer (1988) and 2D simulations with D-GeoFlow (Pol, 2023), this scales as $H_c/L \propto L^{-1/3}$. A 3D analysis without primary erosion (Van Beek et al., 2022) found an exponent of $-1/4$, and in this study we found an exponent of $-1/2$ for 3D domains. At small scale, 3D experiments and simulations already give a lower critical head compared to the current 2D prediction by Sellmeijer et al. (2011). With a stronger scale effect, this difference between 2D and 3D increases even more at larger scale (field scale). However, this result depends on assumptions like the constant $w/a$ ratio. Hence it is essential to better understand the processes behind this scale effect and verify predictions with multi-scale experiments.

With respect to the predicted pipe length development over time, we conclude that the model can reproduce the different stages of pipe growth reasonably well when the erosion coefficient $C_e$ is calibrated. Calibration of the small-scale and large-scale experiments yields consistent values of 0.016 and 0.014, respectively. However, when $C_e$ is estimated directly based on the rate of sediment transport and shear stresses in experiments, this results in higher values of $C_e$ (a factor 25 higher in rectangular flume experiments and a factor 5 higher in small-scale piping experiments). This may be partly explained by the simplification of the pipe as straight rectangular channel in the model, which underestimates the volume of sediment to be transported. However, we recognize that much is still unknown about the details of the BEP erosion process and $C_e$ needs to be calibrated with experiments. The model results indicate that the average progression rate, after exceeding the critical pipe length, increases with grain size and degree of overloading and decreases with scale, which is consistent with experimental observations.

Although the simulated small-scale experiments can be predicted well by the model, we recommend to validate the model more thoroughly on a larger set of experiments, especially those on larger scales and with measurements of the pipe geometry.

## CRediT authorship contribution statement

**Johannes C. Pol:** Conceptualization, Investigation, Methodology, Visualization, Writing – original draft. **Aron Noordam:** Methodology, Software, Visualization, Writing – review & editing. **Willem Kanning:** Investigation, Methodology, Supervision, Writing – review & editing.

## Declaration of competing interest

The authors declare that they have no known competing financial interests or personal relationships that could have appeared to influence the work reported in this paper.

## Data availability

Data will be made available on request.

## Acknowledgments

This work is part of the research programme All-Risk which is (partly) funded by the Netherlands Organisation for Scientific Research (NWO), Domain Applied and Engineering Sciences, with grant number P15-21D.

## Appendix. Results of all simulations

See Tables A.4–A.6.

**Table A.4**
DgFlow simulations for critical conditions.

| $L$ [m] | Sand | Exit | $w/a$ | $i_{tip,c}$ | $H_c$ [m] |
|---|---|---|---|---|---|
| 0.9 | S22 | Hole | 20 | 0.7 | 0.084 |
| 0.9 | S22 | Plane | 20 | 0.7 | 0.158 |
| 3 | S22 | Hole | 20 | 0.7 | 0.144 |
| 3 | S22 | Hole | 20 | 0.7/1.4[a] | 0.182 |
| 3 | S22 | Hole | 30 | 0.7 | 0.157 |
| 3 | S22 | Hole | 67 | 0.7 | 0.182 |
| 3 | S23 | Hole | 20 | 0.7 | 0.170 |
| 3 | S32 | Hole | 20 | 0.7 | 0.151 |
| 3 | S33 | Hole | 20 | 0.7 | 0.178 |
| 3 | S42 | Hole | 20 | 0.7 | 0.153 |
| 3 | S43 | Hole | 20 | 0.7 | 0.184 |
| 3 | S22 | Plane | 20 | 0.7 | 0.284 |
| 9 | S22 | Hole | 20 | 0.2 | 0.254 |
| 9 | S22 | Hole | 200 | 0.2 | 0.424 |
| 9 | S22 | Hole | 43 | 0.2 | 0.304 |
| 9 | S22 | Plane | 20 | 0.2 | 0.376 |
| 30 | S22 | Hole | 20 | 0.2 | 0.470 |
| 30 | S22 | Hole | 115 | 0.2 | 0.693 |
| 30 | S22 | Hole | 64 | 0.2 | 0.607 |
| 30 | S22 | Hole | 667 | 0.2 | 1.047 |
| 30 | S32 | Hole | 20 | 0.2 | 0.501 |
| 30 | S42 | Hole | 20 | 0.2 | 0.501 |
| 30 | S22 | Plane | 20 | 0.2 | 0.764 |
| 90 | S22 | Hole | 20 | 0.15 | 0.864 |
| 90 | S22 | Hole | 2000 | 0.15 | 2.457 |
| 90 | S22 | Hole | 93 | 0.15 | 1.188 |
| 90 | S22 | Plane | 20 | 0.15 | 1.294 |

[a] Local barrier with $i_{tip,c} = 1.4$.

**Table A.5**
DgFlow simulations for time-dependent pipe progression.

| $L$ [m] | Sand | Exit | $w/a$ [–] | $i_{tip,c}$ [–] | $C_e$ [–] | Overload [%] | $H_c$ [m] | $\mathrm{d}l/\mathrm{d}t$ [m/s] |
|---|---|---|---|---|---|---|---|---|
| 0.9 | S22 | Hole | 20 | 0.7 | 0.080 | 5 | 0.084 | $1.05 \cdot 10^{-4}$ |
| 0.9 | S22 | Hole | 20 | 0.7 | 0.080 | 10 | 0.084 | $1.54 \cdot 10^{-4}$ |
| 0.9 | S22 | Hole | 20 | 0.7 | 0.080 | 20 | 0.084 | $2.28 \cdot 10^{-4}$ |
| 0.9 | S22 | Hole | 20 | 0.7 | 0.080 | 30 | 0.084 | $2.94 \cdot 10^{-4}$ |
| 0.9 | S22 | Hole | 20 | 0.7 | 0.080 | 40 | 0.084 | $3.62 \cdot 10^{-4}$ |
| 0.9 | S22 | Plane | 20 | 0.7 | 0.080 | 10 | 0.158 | $7.64 \cdot 10^{-4}$ |
| 3 | S22 | Hole | 20 | 0.7 | 0.008 | 10 | 0.144 | $7.10 \cdot 10^{-6}$ |
| 3 | S22 | Hole | 20 | 0.7 | 0.008 | 40 | 0.144 | $1.64 \cdot 10^{-5}$ |
| 3 | S22 | Hole | 20 | 0.7 | 0.040 | 10 | 0.144 | $3.54 \cdot 10^{-5}$ |
| 3 | S22 | Hole | 20 | 0.7 | 0.040 | 40 | 0.144 | $8.10 \cdot 10^{-5}$ |
| 3 | S22 | Hole | 20 | 0.7 | 0.080 | 5 | 0.144 | $5.65 \cdot 10^{-5}$ |
| 3 | S22 | Hole | 20 | 0.7 | 0.080 | 10 | 0.144 | $7.08 \cdot 10^{-5}$ |
| 3 | S22 | Hole | 20 | 0.7 | 0.080 | 20 | 0.144 | $1.02 \cdot 10^{-4}$ |
| 3 | S22 | Hole | 20 | 0.7 | 0.080 | 30 | 0.144 | $1.31 \cdot 10^{-4}$ |
| 3 | S22 | Hole | 20 | 0.7 | 0.080 | 40 | 0.144 | $1.62 \cdot 10^{-4}$ |
| 3 | S22 | Hole | 20 | 0.7 | 0.160 | 10 | 0.144 | $1.46 \cdot 10^{-4}$ |
| 3 | S22 | Hole | 20 | 0.7 | 0.160 | 40 | 0.144 | $3.36 \cdot 10^{-4}$ |
| 3 | S22 | Hole | 30 | 0.7 | 0.080 | 10 | 0.157 | $7.95 \cdot 10^{-5}$ |
| 3 | S22 | Plane | 20 | 0.7 | 0.080 | 10 | 0.284 | $3.61 \cdot 10^{-4}$ |
| 3 | S22 | Plane | 20 | 0.7 | 0.080 | 40 | 0.284 | $8.20 \cdot 10^{-4}$ |
| 3 | S23 | Hole | 20 | 0.7 | 0.080 | 10 | 0.170 | $8.48 \cdot 10^{-5}$ |
| 3 | S32 | Hole | 20 | 0.7 | 0.080 | 10 | 0.151 | $1.52 \cdot 10^{-4}$ |
| 3 | S33 | Hole | 20 | 0.7 | 0.080 | 10 | 0.178 | $1.69 \cdot 10^{-4}$ |
| 3 | S42 | Hole | 20 | 0.7 | 0.008 | 10 | 0.153 | $2.11 \cdot 10^{-5}$ |
| 3 | S42 | Hole | 20 | 0.7 | 0.040 | 10 | 0.153 | $1.22 \cdot 10^{-4}$ |
| 3 | S42 | Hole | 20 | 0.7 | 0.080 | 5 | 0.153 | $1.82 \cdot 10^{-4}$ |
| 3 | S42 | Hole | 20 | 0.7 | 0.080 | 10 | 0.153 | $2.64 \cdot 10^{-4}$ |
| 3 | S42 | Hole | 20 | 0.7 | 0.080 | 20 | 0.153 | $3.86 \cdot 10^{-4}$ |
| 3 | S42 | Hole | 20 | 0.7 | 0.080 | 30 | 0.153 | $5.21 \cdot 10^{-4}$ |
| 3 | S42 | Hole | 20 | 0.7 | 0.080 | 40 | 0.153 | $9.67 \cdot 10^{-4}$ |
| 3 | S43 | Hole | 20 | 0.7 | 0.080 | 10 | 0.184 | $3.04 \cdot 10^{-4}$ |
| 3 | S42 | Hole | 20 | 0.7 | 0.008 | 40 | 0.153 | $5.42 \cdot 10^{-5}$ |
| 3 | S42 | Hole | 20 | 0.7 | 0.040 | 40 | 0.153 | $2.81 \cdot 10^{-4}$ |
| 9 | S22 | Hole | 20 | 0.2 | 0.080 | 5 | 0.254 | $4.62 \cdot 10^{-5}$ |
| 9 | S22 | Hole | 20 | 0.2 | 0.080 | 10 | 0.254 | $5.47 \cdot 10^{-5}$ |
| 9 | S22 | Hole | 20 | 0.2 | 0.080 | 20 | 0.254 | $7.24 \cdot 10^{-5}$ |
| 9 | S22 | Hole | 20 | 0.2 | 0.080 | 30 | 0.254 | $9.19 \cdot 10^{-5}$ |
| 9 | S22 | Hole | 20 | 0.2 | 0.080 | 40 | 0.254 | $1.11 \cdot 10^{-4}$ |
| 9 | S22 | Hole | 43 | 0.2 | 0.080 | 10 | 0.304 | $6.80 \cdot 10^{-5}$ |
| 9 | S22 | Plane | 20 | 0.2 | 0.080 | 10 | 0.376 | $1.21 \cdot 10^{-4}$ |
| 30 | S22 | Hole | 20 | 0.2 | 0.080 | 5 | 0.470 | $2.43 \cdot 10^{-5}$ |
| 30 | S22 | Hole | 20 | 0.2 | 0.080 | 10 | 0.470 | $2.91 \cdot 10^{-5}$ |
| 30 | S22 | Hole | 20 | 0.2 | 0.080 | 20 | 0.470 | $3.83 \cdot 10^{-5}$ |
| 30 | S22 | Hole | 20 | 0.2 | 0.080 | 30 | 0.470 | $4.78 \cdot 10^{-5}$ |
| 30 | S22 | Hole | 20 | 0.2 | 0.080 | 40 | 0.470 | $5.78 \cdot 10^{-5}$ |
| 30 | S22 | Hole | 20 | 0.2 | 0.160 | 10 | 0.470 | $5.98 \cdot 10^{-5}$ |
| 30 | S22 | Hole | 20 | 0.2 | 0.160 | 40 | 0.470 | $1.24 \cdot 10^{-4}$ |
| 30 | S22 | Hole | 64 | 0.2 | 0.080 | 10 | 0.607 | $3.54 \cdot 10^{-5}$ |
| 30 | S22 | Hole | 115 | 0.2 | 0.080 | 10 | 0.693 | $3.91 \cdot 10^{-5}$ |
| 30 | S22 | Hole | 667 | 0.2 | 0.080 | 10 | 1.047 | $5.59 \cdot 10^{-5}$ |
| 30 | S22 | Plane | 20 | 0.2 | 0.080 | 10 | 0.764 | $7.61 \cdot 10^{-5}$ |
| 30 | S22 | Plane | 20 | 0.2 | 0.080 | 40 | 0.764 | $1.26 \cdot 10^{-4}$ |
| 30 | S32 | Hole | 20 | 0.2 | 0.080 | 10 | 0.501 | $6.06 \cdot 10^{-5}$ |
| 30 | S42 | Hole | 20 | 0.2 | 0.008 | 10 | 0.501 | $8.79 \cdot 10^{-6}$ |
| 30 | S42 | Hole | 20 | 0.2 | 0.040 | 10 | 0.501 | $4.54 \cdot 10^{-5}$ |
| 30 | S42 | Hole | 20 | 0.2 | 0.080 | 10 | 0.501 | $1.01 \cdot 10^{-4}$ |
| 30 | S42 | Hole | 20 | 0.2 | 0.080 | 40 | 0.501 | $3.85 \cdot 10^{-4}$ |
| 30 | S42 | Hole | 20 | 0.2 | 0.008 | 40 | 0.501 | $1.85 \cdot 10^{-5}$ |
| 30 | S42 | Hole | 20 | 0.2 | 0.040 | 40 | 0.501 | $9.49 \cdot 10^{-5}$ |
| 90 | S22 | Hole | 20 | 0.15 | 0.080 | 5 | 0.864 | $1.72 \cdot 10^{-5}$ |
| 90 | S22 | Hole | 20 | 0.15 | 0.080 | 10 | 0.864 | $2.01 \cdot 10^{-5}$ |
| 90 | S22 | Hole | 20 | 0.15 | 0.080 | 20 | 0.864 | $2.60 \cdot 10^{-5}$ |
| 90 | S22 | Hole | 20 | 0.15 | 0.080 | 30 | 0.864 | $3.23 \cdot 10^{-5}$ |
| 90 | S22 | Hole | 20 | 0.15 | 0.080 | 40 | 0.864 | $3.88 \cdot 10^{-5}$ |
| 90 | S22 | Hole | 93 | 0.15 | 0.080 | 10 | 1.188 | $2.52 \cdot 10^{-5}$ |
| 90 | S22 | Plane | 20 | 0.15 | 0.080 | 10 | 1.294 | $4.14 \cdot 10^{-5}$ |

**Table A.6**
DgFlow simulations for time-dependent pipe progression: sensitivity analyses. All cases with $L = 3$ m, S22 sand, hole-exit, $w/a = 20$, $C_e = 0.08$ and 10% overload.

| Analysis | $\Delta t$ [s] | mPicard | $i_{tip,c}$ [–] | $H_c$ [m] | $\mathrm{d}l/\mathrm{d}t$ [m/s] |
|---|---|---|---|---|---|
| Reference | 10 | 2000 | 0.7 | 0.144 | $7.08 \cdot 10^{-5}$ |
| Barrier | 10 | 2000 | 1.4 | 0.182 | $1.63 \cdot 10^{-4}$ |
| Timestep | 5 | 2000 | 0.7 | 0.144 | $6.93 \cdot 10^{-5}$ |
| Timestep | 20 | 2000 | 0.7 | 0.144 | $7.38 \cdot 10^{-5}$ |
| mPicard | 10 | 100 | 0.7 | 0.144 | $7.15 \cdot 10^{-5}$ |
| mPicard | 10 | 200 | 0.7 | 0.144 | $7.16 \cdot 10^{-5}$ |
| mPicard | 10 | 500 | 0.7 | 0.144 | $7.16 \cdot 10^{-5}$ |
| mPicard | 10 | 1000 | 0.7 | 0.144 | $7.10 \cdot 10^{-5}$ |
| mPicard | 10 | 4000 | 0.7 | 0.144 | $7.06 \cdot 10^{-5}$ |

## References

Allan, R., 2018. Backward Erosion Piping (Ph.D. thesis). University of New South Wales.

Bligh, W.G., 1910. Dams, barrages and weirs on porous foundations. Eng. News 64 (26), 708–710.

Callari, C., Pol, J.C., 2022. Numerical interpretation of regressive localized internal erosion in a real-scale levee physical model. Geomech. Energy Environ. 32, 100395.

Den Rooijen, H., 1992. Literatuuronderzoek Doorlatendheid-Korrelkarakterisitieken. Technical Report CO-317710/7, Grondmechanica Delft.

Foster, M., Fell, R., Spannagle, M., 2000. The statistics of embankment dam failures and accidents. Can. Geotech. J. 37 (5), 1000–1024.

Fujisawa, K., Murakami, A., Nishimura, S.-I., 2010. Numerical analysis of the erosion and the transport of fine particles within soils leading to the piping phenomenon. Soils Found. 50 (4), 471–482.

Hanses, U.K., 1985. Zur Mechanik der Entwicklung von Erosionskanälen in geschichtetem Untergrund unter Stauanlagen. Universitätsbibliothek der TU Berlin, Berlin.

Hoffmans, G.J.C.M., 2022. Influence of hydraulic flow regime on backward erosion piping. J. Hydraul. Res. 60 (4), 667–674.

Kanning, W., 2012. The weakest link (Ph.D. thesis). Delft Technical University.

Kézdi, A., 1979. Soil Physics: Selected Topics. In: Developments in geotechnical engineering, vol. 25, Elsevier, Amsterdam.

Miesel, D., 1977. Untersuchungen zum problem der rückschreitenden erosion als ursache des hydraulischen grundbruches in böden mit inhomogener schichtfolge. In: Veröffent-Lichungen Des Grundbauinstitutes Der Technischen UniversitäT Berlin. Vol. 1, Technischen Universität Berlin, Berlin, pp. 56–71.

Okamura, M., Tsuyuguchi, Y., Izumi, N., Maeda, K., 2022. Centrifuge modeling of scale effect on hydraulic gradient of backward erosion piping in uniform aquifer under river levees. Soils Found. 62 (5), 101214.

Pol, J.C., 2022. Time-dependent development of Backward Erosion Piping (Ph.D. thesis). Delft University of Technology.

Pol, J.C., 2023. Discussion of 'influence of erosion on piping in terms of field conditions' by G. Hoffmans. J. Hydraul. Res. 61 (1), 162–164.

Pol, J.C., Kanning, W., van Beek, V.M., Robbins, B.A., Jonkman, S.N., 2022. Temporal evolution of backward erosion piping in small-scale experiments. Acta Geotech. 17 (10), 4555–4576.

Pol, J.C., Kanning, W., Jonkman, S.N., 2021. Temporal development of backward erosion piping in a large-scale experiment. J. Geotech. Geoenviron. Eng. 147 (2), 04020168.

Pol, J.C., Van Beek, V.M., Kanning, W., Jonkman, S.N., 2019. Progression rate of backward erosion piping in laboratory experiments and reliability analysis. In: Ching, J., Li, D., Zhang, J. (Eds.), 7th International Symposium on Geotechnical Safety and Risk (ISGSR). Research Publishing, Tapei, pp. 764–769.

Riha, J., Petrula, L., 2023. Experimental research on backward erosion piping progression. Water 15 (15), 2749.

Robbins, B.A., 2022. Finite Element Modeling of Backward Erosion Piping (Ph.D. thesis). Colorado School of Mines.

Robbins, B.A., van Beek, V.M., Pol, J.C., Griffiths, D.V., 2022. Errors in finite element analysis of backward erosion piping. Geomech. Energy Environ. 31, 100331.

Robbins, B.A., Griffiths, D.V., 2018. Modelling of backward erosion piping in two-and three-dimensional domains. In: Bonelli, S., Jommi, C., Sterpi, D. (Eds.), European Working Group on Internal Erosion. Springer, pp. 149–158.

Robbins, B.A., Griffiths, D.V., 2021. A two-dimensional, adaptive finite element approach for simulation of backward erosion piping. Comput. Geotech. 129, 103820.

Robbins, B., Montalvo-Bartolomei, A., Griffiths, D., 2020. Analyses of backward erosion progression rates from small-scale flume experiments. J. Geotech. Geoenviron. Eng. 146 (9), 04020093.

Robbins, B.A., Van Beek, V.M., Lopez-Soto, J.F., Montalvo-Bartolomei, A.M., Murphy, J., 2017. A novel laboratory test for backward erosion piping. Int J Phys Modell Geotech 18 (5), 266–279.

Rosenbrand, E., van Beek, V., Bezuijen, A., 2021. Numerical modelling of the resistance of the coarse sand barrier against backward erosion piping. Géotechnique 72 (6), 1–29.

Rotunno, A.F., Callari, C., Froiio, F., 2019. A finite element method for localized erosion in porous media with applications to backward piping in levees. Int. J. Numer. Anal. Methods Geomech. 43 (1), 293–316.

Schmertmann, J., 2000. 'No-filter factor of safety against piping through sands'. In: Silva, F., Kavazanjian, E. (Eds.), Judgment and Innovation. ASCE, Reston, VA, USA, pp. 65–105.

Sellmeijer, J.B., 1988. On the mechanism of piping under impervious structures (Ph.D. thesis). Delft University of Technology.

Sellmeijer, H., de la Cruz, J.L., van Beek, V.M., Knoeff, H., 2011. Fine-tuning of the backward erosion piping model through small-scale, medium-scale and ijkdijk experiments. Eur. J. Environ. Civ. Eng. 15 (8), 1139–1154.

Tran, D.K., Froiio, F., Vincens, E., Prime, N., Callari, C., 2017. Numerical modelling of backward front propagation in piping erosion by DEM-LBM coupling. Eur. J. Environ. Civ. Eng. 21 (7–8), 960–987.

Van Beek, V.M., 2015. Backward erosion piping: Initiation and progression (Ph.D. thesis). Delft University of Technology.

Van Beek, V., Robbins, B., Rosenbrand, E., van Esch, J., 2022. 3D modelling of backward erosion piping experiments. Geomech. Energy Environ. 31, 100375.

van Esch, J.M., 2014. Groundwater Flow Simulator DgFlow 3D Validation Piping Module (1209435-006-GEO-0001). Technical Report, Deltares.

van Esch, J.M., 2015. WTI 2017: Toetsregel Piping. Validation Piping Module DgFlow (Report Including Primary Erosion). Technical Report, Deltares.

van Esch, J.M., Sellmeijer, J.B., Stolle, D., 2013. Modeling transient groundwater flow and piping under dikes and dams. In: Pietruszczak, S., Pande, G. (Eds.), 3rd International Symposium on Computational Geomechanics (ComGeo III). Vol. 9, Taylor I& Francis, Krakow, Poland.

Vandenboer, K., 2019. A study on the mechanisms of backward erosion piping (Ph.D. thesis). Ghent University.

Vandenboer, K., van Beek, V., Bezuijen, A., 2014. 3D finite element method (FEM) simulation of groundwater flow during backward erosion piping. Front. Struct. Civ. Eng. 8 (2), 160–166.

Vandenboer, K., van Beek, V.M., Bezuijen, A., 2018. 3D character of backward erosion piping. Géotechnique 68 (1), 86–90.

Vandenboer, K., Celette, F., Bezuijen, A., 2019. The effect of sudden critical and supercritical hydraulic loads on backward erosion piping: small-scale experiments. Acta Geotech. 14 (3), 783–794.

Wang, D.-y., Fu, X.-d., Jie, Y.-x., Dong, W.-j., Hu, D., 2014. Simulation of pipe progression in a levee foundation with coupled seepage and pipe flow domains. Soils Found. 54 (5), 974–984.

Wewer, M., Aguilar-López, J.P., Kok, M., Bogaard, T., 2021. A transient backward erosion piping model based on laminar flow transport equations. Comput. Geotech. 132, 103992.

White, C., 1940. The equilibrium of grains on the bed of a stream. Proc. R. Soc. Lond. Ser. A Math. Phys. Sci. 174 (958), 322–338.

Xiao, Y., Cao, H., Luo, G., 2019a. Experimental investigation of the backward erosion mechanism near the pipe tip. Acta Geotech. 14 (3), 767–781.

Xiao, Y., Cao, H., Luo, G., Zhai, C., 2019b. Modelling seepage flow near the pipe tip. Acta Geotech..

Xiao, Y., Pan, H., Luo, G., 2023. Modelling of flow in backward erosion pipes. Geomech. Energy Environ. 100476.